IEEE Access
Multidisciplinary | Rapid Review | Open Access Journal

Received April 9, 2020, accepted April 28, 2020, date of publication May 11, 2020, date of current version May 22, 2020.

Digital Object Identifier 10.1109/ACCESS.2020.2993698

Spherical mm-Wave/THz Antenna Measurement System

BENEDIKT SIEVERT, (Member, IEEE), JAN TARO SVEJDA, (Member, IEEE), DANIEL ERNI, (Member, IEEE), AND ANDREAS RENNINGS, (Member, IEEE)

General and Theoretical Electrical Engineering (ATE), Faculty of Engineering, CENIDE–Center for Nanointegration Duisburg-Essen, University of Duisburg-Essen, 47048 Duisburg, Germany

Corresponding author: Benedikt Sievert (benedikt.sievert@uni-due.de)

This work was supported by the Deutsche Forschungsgemeinschaft (DFG, German Research Foundation)—TRR 196 MARIE under Grant 287022738. The authors acknowledge support by the Open Access Publication Fund of the University of Duisburg-Essen.

ABSTRACT This paper presents an automatic characterization system for mm-wave antennas based on a spherical positioning system. It features network-analysis based far-field- and S-parameter measurement of probe- and waveguide-fed antennas between 220 GHz and 330 GHz, expandable down to 75 GHz. In either case, the antenna under test (AUT) is fixed in the center of a spherical coordinate system and fed by an appropriate feeding structure, whereas the receiving antenna is moved along the surface of a hemisphere. Since the movement of the receiving antenna is inherently limited to constant radii, the measurement of amplitude and phase far-field-pattern is possible in principle. Additionally to the measurement results of an open-ended waveguide as AUT, this paper describes two methods for the self-characterization of possible systematic and stochastic measurement uncertainties. On one hand, repetitive measurements along a constant trace are carried out to obtain information about the stochastic uncertainty of far-field measurements. On the other hand, a synthetic aperture radar (SAR)-approach is used to characterize possible unwanted reflections within the measurement setup. Finally, the insight obtained from both antenna measurements and self-characterization is concluded into performance parameters of the presented measurement approach.

INDEX TERMS Antenna measurements, antenna radiation patterns, millimeter wave measurements, millimeter wave technology.

I. INTRODUCTION

The monotonically increasing demand on data rates for communications, resolution for localization and finer details for characterization intrinsically requires a large absolute bandwidth. Since the useable absolute bandwidth increases for a constant relative bandwidth with rising frequency, there is a huge interest in systems, channel-estimations, and measurements within the mm-wave regime. In all cases, antennas of various types couple from RF-frontends into free-space and vice versa. The demand for characterizing the antennas for both measurement devices and tailored systems comes along with the estimation of the system performance, the error-characterization, and device-modeling. This paper presents an automated antenna measurement system dedicated to characterizing mm-wave on-chip antennas in terms of their radiated far-fields and S-parameters.

Other systems measuring in spherical coordinates have been presented before; however, a multitude of them was designed for measuring cut planes at frequencies around 60 GHz [1], [2]. Measurement systems exceeding 100 GHz were able to measure cut planes in an anechoic chamber [3] or built up quasi-optical [4]. The system presented in [5] has been modified by the use of mixers allowing for frequencies up to 140 GHz [6], and the system in [7] was modified to allow for measurements up to 325 GHz [8]. The mixers or detectors are often located in proximity to the receiving antenna [6], [9]; however, solutions exist where waveguides are used as a combined mechanical positioner and waveguiding structure [10], [11]. To obtain 3D measurements above 100 GHz, robotic arms are a common choice due to their flexibility in use and market availability, as in [9], [12]. Furthermore, systems providing measurements only in cartesian

The associate editor coordinating the review of this manuscript and approving it for publication was Mingchun Tang.

coordinates for antenna characterization and scattering investigations exist [13]. A comprehensive comparison of mm-wave antenna characterization systems is presented in tabular form in [14].

The characteristic feature of the here presented system is the hemispherical plastic positioning system utilized to measure far-fields in a spherical coordinate system. As in the early approach in [15], this system is built especially for radiation pattern measurements in spherical coordinates utilizing mostly non-metallic components; however, the presented system increases the upper frequency band up to 330 GHz, consistently allows for both sufficient mechanical stability as well as minimizing the distortion of measurements, and aims for measuring fully complex (magnitude and phase) 3D radiation pattern within the upper hemisphere. This non-metallic but substantial mechanical stable system is to the best of the authors' knowledge unique in the field, allowing for precise elevation and azimuth measurements in the upper hemisphere while maintaining a constant radius, which is necessary for phase-correct measurements, by design. Besides exemplary measurements demonstrating the feasibility of the presented system, a set of methods for the self-characterization of the system is presented and discussed.

This paper is separated into the following sections. At first, Section II explains the general design of the measurement setup, including material considerations and mechanical limitations. Secondly, Section III describes the implemented measurement methods and combinations including network-analysis operation, feeding methods, and mechanical positioning. As a first justification of the design choices, Section IV describes a synthetic aperture radar (SAR) inspired method to visualize undesired reflections within the reach of the measurement setup. The following Section V discusses the ability of the presented system to accurately measure not only amplitude but also phase patterns. After these preliminary evaluations, the far-field measurement of an open-ended rectangular waveguide is analyzed and compared to full-wave simulations in Section VI. Finally, the paper is concluded in Section VII.

II. DESIGN OF THE MEASUREMENT SYSTEM

The mm-wave antenna measurement setup is depicted in a distance shot in Fig. 1 (a), in a detail view in Fig. 1 (b), in profile and top view of the CAD model (c, d). The coordinate system throughout used within this paper is depicted as an overlay, where the x-y-plane lays horizontally and the z-axis points skywards. The explanation of the system follows a bottom-to-top approach to clarify dependencies. Since vibrations can dramatically degenerate mm-wave measurements in general and especially RF-probe based on-wafer measurements in particular, the whole system uses an air-suspended optical table as a baseplate. Additionally to the vibrational decoupling of the remaining room, standard optical- and mm-wave components can be easily fixed, shifted, and removed on the optical table. Apart from the optical table, the system components which can be separated

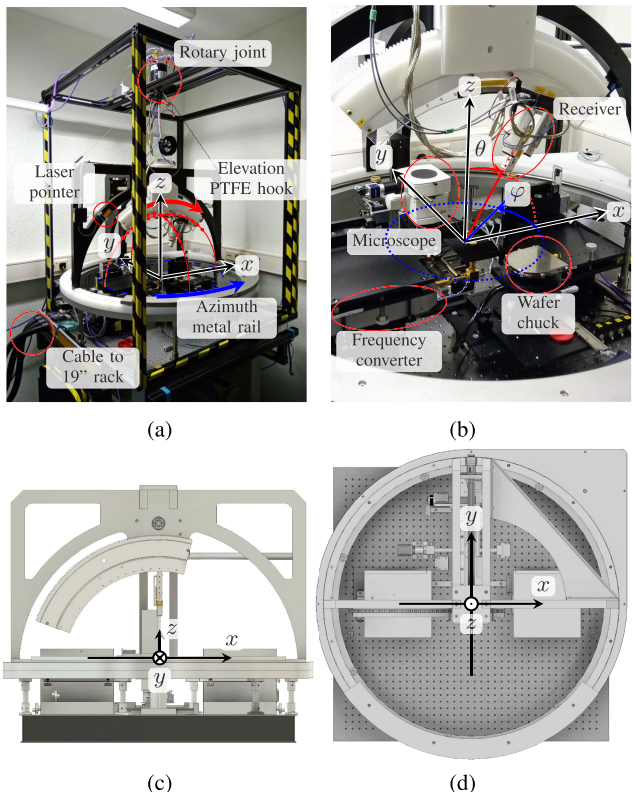

FIGURE 1. Photo of the measurement system in distance shot (a) and detail-view (b) as well as drawings from the CAD model in the side view (c) and top view (d). The coordinate system, as well as important components, are labeled within the pictures. The red dotted line in (a) represents exemplary measurement paths to obtain elevation cut planes.

are stacked in a 19-inch industrial rack right next to the system. These components involve the control and drive unit of the positioning system, the vector network analyzer (VNA) as well as the local oscillator (LO) source, DC power supplies, and the main control personal computer. All RF coaxial cables, DC cables, and vacuum tubes passed over from the 19-inch rack onto the table are mounted loosely on both sides (cf. Fig. 1 (a)).

The optical table supports a non-metallic (plastic wood composite material) rectangular frame (marked with yellow-black warning tape) used for cable guidance. Inside the frame, the spherical positioning system is mounted on the optical table. It enables the positioning of the receiver in azimuth and elevation, i.e. in spherical coordinates. A crucial requirement of this custom-built system provided by Demcon Systec Industrial Systems was the utilization of non-metallic parts in the upper hemisphere to intrinsically suppress strong reflections without cladding the whole system with absorbers. The use of large metallic positioning systems has been shown to create ripples in radiation pattern due to multiple reflections within the measured diagrams if the systems are not covered by absorbing materials [9]. As an outcome, the receiver, the stepper motor for the elevation plane, and the supplying cables are the only parts consisting of metal within the construction. In comparison to systems which show a large

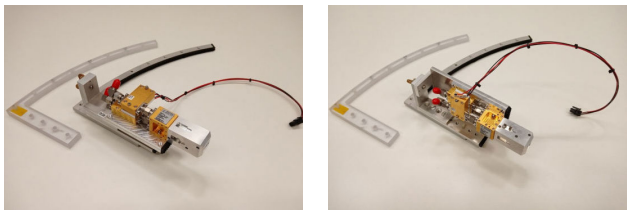

FIGURE 2. Extension hook made from polycarbonate (transparent) and absorber-cladded-aluminum. The latter one supports the receiving frequency converter mounted in φ- (a) and θ- (b) polarization.

leverage effect on small diameter bearings resulting in a large mechanical stress and positioning inaccuracies, which needs to be evaluated [16], this system utilizes a large metal rail with heavy spot compensation as an azimuthal bearing. However, the metal parts of the azimuthal rail are considered negligible, as they are located below the equator ($\theta > 90°$) of the system. To prevent the twisting of DC and RF cables, where the latter suffer from twisting in terms of phase-stability and durability, a 2-channel RF- and a 16-channel DC-rotary joint are mounted coaxially aligned with the z-axis of the system on the composite material frame, allowing for unlimited revolutions in the azimuthal direction. In the orthogonal direction, the movement in elevation is enabled by the PTFE hook, where the RF cables are supported in a single loop to prevent sharp bends. The hook is limited in its elevation range to $\theta_{\max} = 51°$ to prevent collisions. Nevertheless, a full elevation half-plane up to $\theta = 90°$ can be measured, as it will be shown later.

Two cartesian motor-driven large area manipulators, where each covers a space of 60 mm × 45 mm × 150 mm ($x \times y \times z$), carry and position the frequency converters in 3 dimensions on the optical table to enable a flexible waveguide and RF-Probe alignment. The frequency converters are used for generating and receiving the mm-wave signal guided by rectangular waveguides. A 100 mm wafer chuck can be manually shifted and fixed in the x-y-plane. It is located in the center of the system for on-chip measurements and can be shifted out of the center to allow for waveguide-based measurements (cf. Fig. 1 (b)). The origin of the system is optically indicated by a laser beam. A camera-based microscope necessary for contacting wafer-probes on the chip is mounted on a third 3D, cartesian large area manipulator covering a space of 180mm × 260 mm × 200 mm and enabling to drive the microscope from the covered position (cf. Fig. 1 (b)) to the active position above the centered chuck (cf. Fig. 3 (b)) with low vibration. Within the active position, one can observe the probing process, but even for the S-parameter measurement it should be placed in the covered position, as the proximity of the microscope was shown to have a strong influence on the input reflection coefficient at 60 GHz [17].

The receiving frequency converter used for far-field measurements is mounted on an extension hook, which extends the limited range of the elevation positioner by enabling a

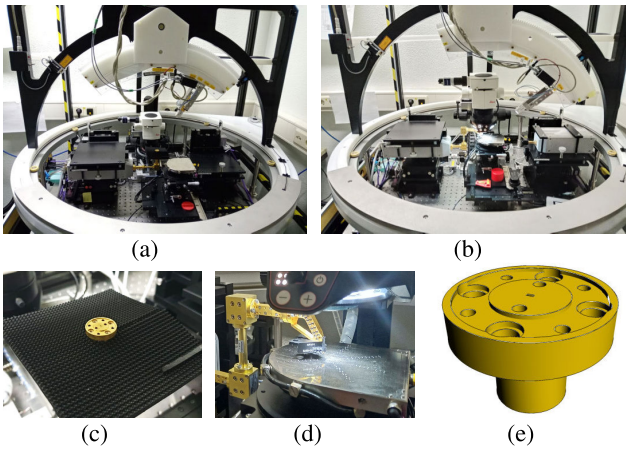

FIGURE 3. Photograph on the measurement system (a) characterizing an open-ended waveguide surrounded by an absorber patch, (c) shows the detail-view. It can be seen that the microscope is in the covered position. (b) shows the observation of the wafer-probe with the microscope above the chuck, (d) shows a close-up view. The receiver needs to be elevated towards $\theta \approx 50°$ in order to prevent collisions of the microscope and the receiver. (e) shows the model of the open-ended waveguide with the UG387 flange utilized for the FDTD simulation.

manual offset θ_{offs}. In an early stage, a polycarbonate (PC) extension hook has been used; however, Section V will show that an absorber-cladded aluminum extension hook increases the performance dramatically. Both hooks are shown in Fig. 2, where Fig. 2 (a) shows the receiver mounted to measure the φ-polarization, and Fig. 2 (b) the θ-polarization. The miniaturized far-field receiver (R&S ZRX330L) is a compact and lightweight version of the housed and stabilized full receiver R&S ZRX330.

III. MEASUREMENT METHODS AND PROCEDURES

The capabilities of measurements carried out with this system involve transmission and reflection measurements with both rectangular waveguides and on-wafer probes. In general, the mm-wave frequency converter (R&S ZC-330) is used as transceiving (TxRx) port 1 in any case. Depending on the measurement task, either no receiver (only S_{11}-measurement), a receiver (R&S ZRX-330) mounted on the optical table (S_{11} and S_{21}), or the miniaturized receiver (R&S ZRX-330L) mounted on the spherical coordinate system (S_{11} and $S_{21,\text{far-field}}$) can be used. For all measurements involving only the frequency converters mounted on the table, a waveguide-based or wafer-based calibration (using two probe tips and a suitable calibration substrate) is possible [17], where the characteristic of the probe itself can be obtained as well [18]. If the on-wafer probe is used, the rectangular waveguide sections are assembled to build an S-shaped waveguide in order to lower the position of the frequency converter on the lefthand side (cf. Fig. 3 (b, d)) enabling larger elevation ranges for the spherical measurement system. There exists a lot of research on the effect of probe tips on the measured far-field pattern, as they may generate own radiation contributions [19], create shadow regions in the far-field pattern due to their large size [20], [21] and

create interference effects due to scattering at the metallic probe [22], which can be even used to localize the scattering center of the probe [20]. Methods for corrections of both of the probe's radiation [23] and shadowing [24] have been presented, which leaves this measurement setup only with the prevention of scattering from the metallic probe. This has been achieved by covering the upright faces of the probe with a thin layer of a mm-wave absorber (cf. Fig. 3 (d)).

Whenever the far-field receiver comes into play, a more antenna-tailored calibration must be used. At first, the calibration can be carried out only for the feeding port, resulting in a characterization of the input mismatch of the waveguide- or wafer-based antenna. In this case, it is assumed that the influence of the hemispherical measurement setup and the receiver on the input-reflection coefficient is negligible. The calculation of the realized gain relies on the comparison of the AUT with a well-known horn antenna. If the insertion losses of the rectangular waveguides differ for the reference antenna and the antenna under test (AUT), e.g. due to the additional S-shaped section, this information needs to be included as well. The realized gain of the antenna under test G_{AUT} thus calculates to [10]

$$G_{\mathrm{AUT}} = G_{\mathrm{Ref}} \left| \frac{S_{21,\mathrm{AUT}}}{S_{21,\mathrm{Ref}}} \right|^2 \cdot \left| \frac{S_{21,\mathrm{WG}\to\mathrm{Ref}}}{S_{21,\mathrm{WG}\to\mathrm{AUT}}} \right|^2, \qquad (1)$$

where G_{Ref} is the known gain of the reference antenna, $S_{21,\mathrm{AUT}}$ and $S_{21,\mathrm{Ref}}$ are the far-field transmission parameters of the antenna under test and the reference antenna, respectively. The difference in waveguide losses can be evaluated in a direct transmission measurement and is considered by comparing the insertion loss of the waveguide section towards the antenna under test $S_{21,\mathrm{WG}\to\mathrm{AUT}}$ and the reference antenna $S_{21,\mathrm{WG}\to\mathrm{Ref}}$. It should be assured that the radiating apertures of both antennas are at the same position, such that the free-space path loss is identical for both measurements.

Setting up the measurement usually involves driving the large area manipulators of the frequency converters and the microscope to the desired positions. The characterization of the input-reflection coefficient S_{11} is carried out without using the spherical coordinate system – except for the elevation of the receiver in order to give place for the microscope (cf. Fig. 3 (b)). For the far-field measurements, the extension hook of the receiver (cf. Fig. 2) can be used to decide on the desired elevation range. Since the spherical positioning system is limited in its elevation range, an offset in 5°-steps can be introduced to the measurement range, as shown in Fig. 4. Here, different offsets are used and the achievable range per offset is highlighted with the shaded domain. It should be noted that the range is inherently not limited to $\theta \leq 85°$, although Fig. 4 (a) creates this impression. The range is in this case for $\varphi = 180°$ limited to $\theta < 85°$ to avoid a collision with the positioner of the frequency extender. In general, e.g. for $\varphi = 0°$ and $\varphi = -90°$, the extension hook allows for an offset of $\Delta\theta|_{\max} = 40°$ resulting in a measurable range of $40° \leq \theta \leq 90°$ (cf. Section VI). The usual case is a measurement with an elevation range $0° \leq \theta \leq 50°$, as shown in Fig. 4 (b), since this case is the most important one for highly directive, broadside radiating antennas. However, measurements at the equatorial plane (cf. Fig. 4 (a)) or with inherent redundancy for error-detection (cf. Fig. 4 (c)) are possible.

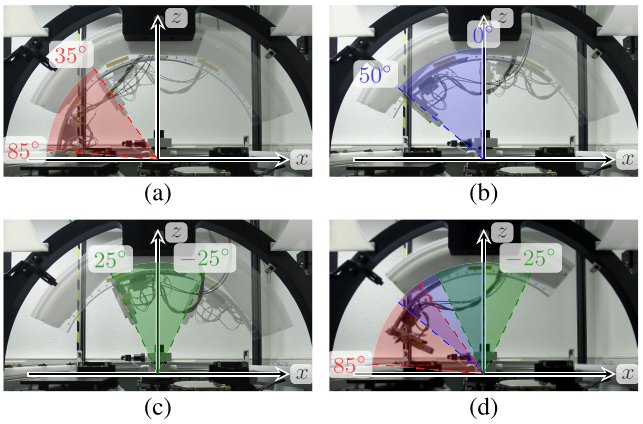

FIGURE 4. Exemplary hook extensions enabling measuring ranges $35° \leq \theta \leq 85°$ (a), $0° \leq \theta \leq 50°$ (b), $-25° \leq \theta \leq 25°$ (c) as well as the combined, overlapping ranges (d). The ranges are emphasized by the graphical overlay of each two photos depicting the receiver in the minimum and maximum position (a-c). (d) shows the receiver at $\theta = 74°$.

IV. SYNTHETIC APERTURE DRIVEN SELF-CHARACTERIZATION

Apart from the actual feasibility of the measurement system, which has been explained in the Sections above, the errors introduced by the measurements need to be identified. Usually, far-field measurement setups are either set up utilizing metal positioning systems cladded with absorbers [9], [25], or low-loss dielectrics to avoid reflections [19]. Besides the secondary observation of reflections, i.e. observing whether measurement data change when adding absorbers [9], the characterization of the reflections caused by the measurement system has been carried out in a time-domain approach [26]. This section aims to describe a mature method for the self-characterization, meaning that the measurement system is used to characterize occurring reflections utilizing the available devices. Along with the practicability of this approach, it contains another extensive benefit. Since the same frequency converters are used for the measurement and the self-characterization, they inherently use the same frequency range for both characterization and measurement. This again implies that each disturbing material, which is not detectable within the utilized frequency range in the characterization, will also not disturb the measurement. Looking at the other way round, absorbers which might be operating nicely at 330 GHz are not necessarily optimal at 110 GHz or 500 GHz. The self-characterization allows for the consideration of exactly these effects at each frequency band. To determine the different reflection contributions of S_{11} at different ranges, the most straightforward approach is to observe the signal in the time-domain.

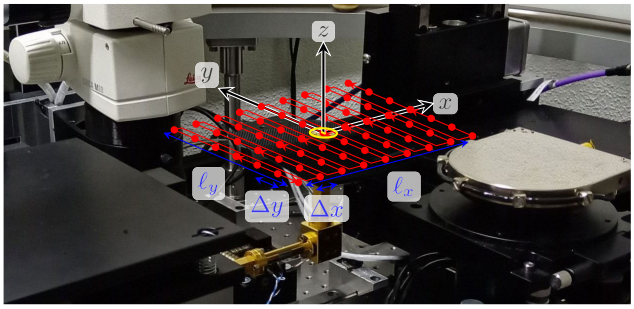

FIGURE 5. Exemplary representation of the measurement path moved along by the waveguide flange for the self-characterization. The actual grid contained 111 by 81 measurement points and is just qualitatively represented by the drawing, the waveguide flange is highlighted in yellow.

TABLE 1. Network-analysis parameters of the SAR-Measurement.

Start Freq. f_{Start}	Stop Freq. f_{End}	Freq. Step Δf	Meas. Bandwidth f_{BW}
220 GHz	330 GHz	0.1 GHz	100 Hz

TABLE 2. Geometrical parameters of the SAR-Measurement.

Number of Steps N_x	N_y	Aperture Length ℓ_x	Aperture Width ℓ_y	Stepsize $\Delta x = \Delta y$
111	81	55 mm	40 mm	0.5 mm

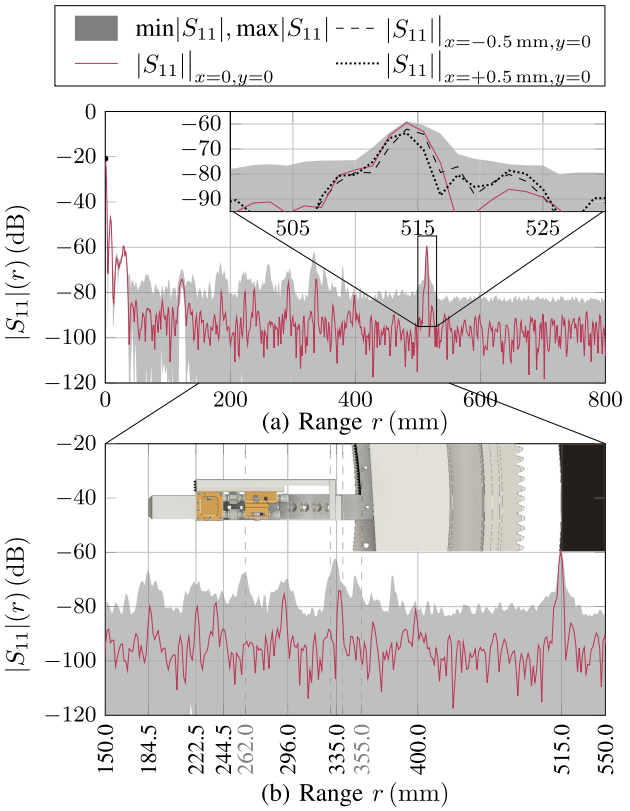

FIGURE 6. Time-domain response of an open-ended waveguide radiating into the upper hemisphere. The min and max refer to all 8891 (81 · 111) measurements within the scope given in Table 2. (a) shows a large range where the inset highlights the reflection at the black arc for different antenna positions, whereas (b) compares the reflection pulse trains to the geometrical distance between receiver and origin.

Fig. 5 shows an open-ended WR3.4 waveguide facing into the upper hemisphere located in the $z = 0$ plane. It is surrounded by a rectangular collar of mm-wave absorber material of ≈ 80 mm $\times$ 80 mm, which is located ≈ 10 mm below the flange (cf. Fig. 3 (c)). The VNA is utilized to measure the input reflection coefficient S_{11} with the parameters given in Table 1. A waveguide calibration (short, offset-short, and load) has been carried out to shift the reference plane onto the waveguide flange. To obtain range estimations from different antenna positions, the open-ended waveguide is moved along a rectangular grid defined by Table 2 and centered around the origin (cf. Fig. 5) by use of the large area manipulator of the frequency converter. The frequency response is transformed into a time-domain response utilizing a Blackman-window in the frequency domain and converted into a free-space distance with the speed of light c_0. The response of the antenna at the origin as well as the respective maximum and minimum values of all measurements are shown in Fig. 6 (a). Although the unambiguous region is much larger, there are no further spikes in the time-domain worth mentioning beyond a distance of 800 mm. The inset shows a detail-view on the region around 515 mm, where a noticeably strong peak, which is still ≈ 40 dB below the input-reflection pulse of the open-ended waveguide, appears. This peak corresponds to the circular black arc of the positioning system, which is designed with a radius of 515 mm. At a first glance, this arc centered around the origin appears to be a structural drawback of the presented spherical measurement system, as it, if the antenna is placed exactly in the origin, focuses all wavefronts back to the origin where these will interfere constructively. Consequently, even though the arc is made of a low-permittivity plastic, it is visible in the time-domain representation. This enables the user to seek the origin of the measurement system with a simple optimization goal: the antenna position with the largest and narrowest peak at $d \approx 515$ mm corresponds to the origin. As mentioned above, the accuracy reachable with this method increases with the use of higher frequency bands and is thus always below the order of the wavelength utilized. To justify this outcome, the inset in Fig. 6 (a) shows the time-domain representations of the signals measured in the neighboring positions $x = \pm 0.5$ mm, which are roughly half a wavelength apart from the origin. It is obvious that the offset positions result both in a reduced amplitude of roughly 3 dB and an increased width of the peak, which means that they are not in the focal point of the black arc. If one wants to determine the origin in both axis, x and y, this optimization can be carried out for both axes independently by rotating the spherical positioning system and thus the black arc to $\varphi = 0°$ and $\varphi = 90°$, respectively.

The other peaks occurring in the time-domain will be discussed in the following. At first, there exists an omnipresent ringing for distances below 50 mm, which is practically

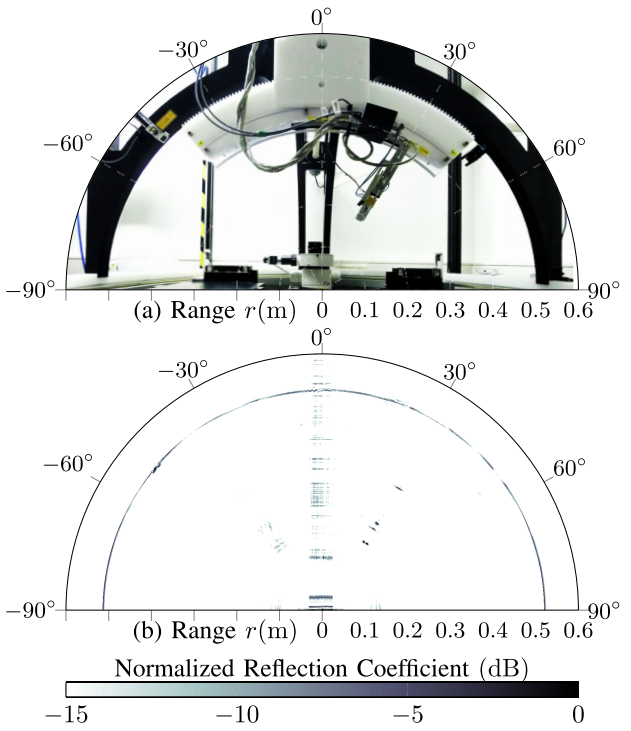

FIGURE 7. Backprojection of the synthetic aperture radar into the *x*-*z*-cut plane with (a) a photograph of the real setup and (b) the corresponding radar-image.

independent from the antenna position. The same holds for the peak at $\approx$ 122 mm, which is also strikingly constant throughout all measurements. As these peaks do not change at the different antenna positions, it is assumed that one sees either an effect of the waveguide flange or imperfections within the calibration, but no reflections corresponding to obstacles in the upper hemisphere above the waveguide flange. Secondly, there exist peaks which seem to change with changing antenna positions, they seem to correspond to targets in a radar sense. Fig. 6 (b) shows a detail-view of the time-domain signal from Fig. 6 (a). All sharp edges existing within the technical drawing of the mounted receiver are mapped to the axis' ticks, a colored sketch of the CAD model is depicted above the time-domain signal and mapped to its geometrical distance to the origin. One can clearly see that the expectation from the technical drawing fits the pulses in the time-domain representation with excellent precision. The gray labels correspond to faces that were expected to cause visible reflections, but the time-domain representation did not show any peaks there. It should be pointed out that the distance $d = 354$ mm corresponds to the absorber-cladded aluminum extension hook depicted in Fig. 4, and that it is effectively hidden by the absorber. The reflection at 400 mm corresponds to the PTFE housing of the bearing for the elevation-axis.

To get a more visual impression of the location of scatterers, a backprojection of the received signals for points in a 2D or 3D space can be carried out [27]. The positioning system was set to an azimuthal angle of $\varphi = 0°$, corresponding to a measurement in the x-z-plane, and an elevation of $\theta = 30°$, such that reflections from the receiver can be easily recognized. A photograph of the observed scene, as well as the calculated reflection coefficients in the x-z-cut plane, are depicted in Fig. 7. Apart from the straight reflections for ranges smaller 150 mm, which correspond to the omnipresent peaks in the time-domain signals, both the black arc of the positioning system as well as the receiver can be recognized in the radar image. One can even recognize an accumulation of stronger reflections at $d = 515$ mm and $\theta = -45°$ due to the fixture of the laser pointer. Concluding this section, the approach of building up this measurement system practically without any metal parts, except for the receiver, cables, and a stepper motor, paid off in terms of low reflections visualized in the time-domain. Apart from the reflection due to the black plastic arc, which can be used to determine the origin of the measurement setup with a precision below a wavelength, practically no reflection worth mentioning occurred. Hence, if one wanted to further suppress these reflections, one would need to clad the reflecting parts of the receiver, except for the antenna itself, with absorbers.

V. PHASE-CENTER INVESTIGATIONS

As the measurements within the last section have shown, the spherical antenna measurement system affects ongoing measurements only with very weak disturbing reflections. This section aims to quantify the repeatability, with which the measurements can be carried out. An extensive uncertainty budged is presented in [28]; however, the evaluation of the phase uncertainty requires extremely precise knowledge about the radial position accuracy and the phase stability of the cables. Although in the context of near-field measurements, the importance of phase-correct measurements as well as the crucial influence of the utilized cables are presented in [29], [30]. The phase change caused by cable lifting and lowering, which is comparable to the movement carried out during the measurement, has been estimated up to 20° deviation at 325 GHz in [25], of course, depending on the type and length of the cable used.

Concerning mechanical repeatability, the radius of the receiver on the hemisphere, i.e. the distance towards the origin, needs to remain unchanged during the measurement. The deviation Δr from the desired constant radius would lead for extreme cases to a change in the transmission amplitude, as the received signal reduces with increased antenna distance. However, as the distance between origin and receiver is about 150 wavelengths at 250 GHz and the deviation is expected to be at the scale of the wavelength, amplitude fading is expected to be practically nonexistent. In contrast to that, the measured phase is much more sensitive even to a deviation below one wavelength, as the phase grows linear according to $2\pi\Delta r/\lambda$. Furthermore, it is expected that the aluminum extension hook shows an improved performance in terms of repeatability due to a larger stiffness compared to the polycarbonate candidate. Here, a two-port measurement

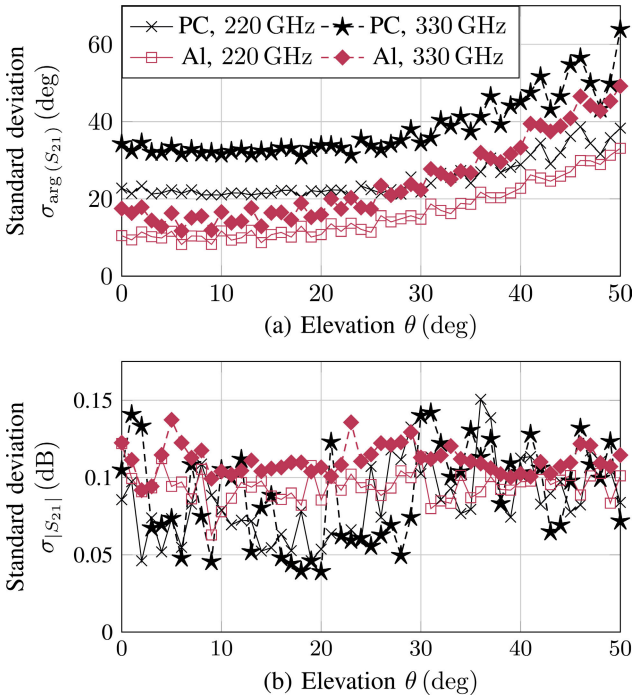

FIGURE 8. Standard deviation of (a) the unwrapped phase of the transmission parameter and (b) the amplitude in decibel for 70 repetitions of an elevation cut $0° \leq \theta \leq 50°$. Shown are two different materials of the extension hook (polycarbonate – PC and aluminum – Al) at the lower and upper bound of the WR3.4-waveguide band.

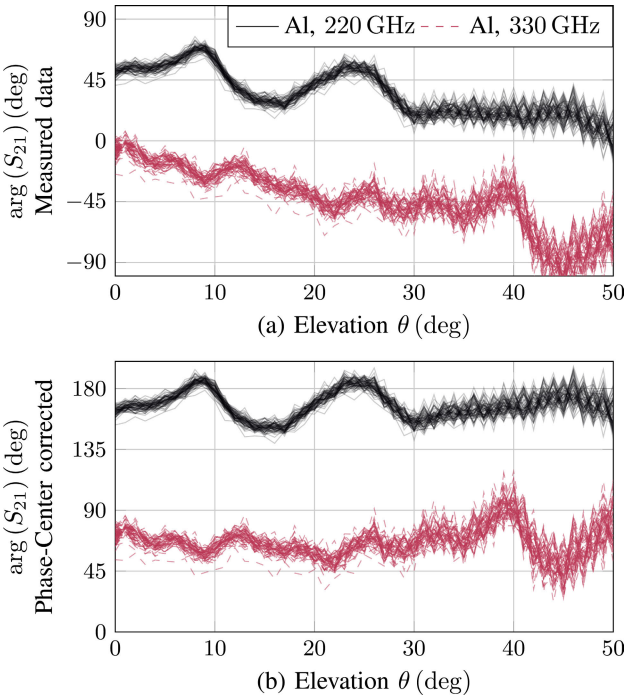

FIGURE 9. Phase of the transmission coefficient S_{21} for 70 repetitions (a) as originally measured and (b) phase-center-corrected with the parameters from Table 3.

is carried out using the open-ended waveguide in the origin of the measurement system as transmitting antenna and the receiver on the spherical positioning system as receiving port. For the fixed azimuth angle $\varphi = 0°$ the elevation angle was varied between $0° \leq \theta \leq 50°$ in steps of $\Delta\theta = 1°$. This measurement along the elevation cut was carried out 70 times using both the polycarbonate (referred to as *PC*) and aluminum extension hook (referred to as *Al*). For each set of measurements, the standard deviations for both the unwrapped phase $\arg(S_{21})$ and amplitude in decibel $|S_{21}|_{\text{dB}}$ of the transmission coefficient have been calculated and are depicted in Fig. 8. Concerning Fig. 8 (a), the standard deviation of the phase shows tendencies concerning frequency, material, and elevation angle. At first one can see that the larger frequency of 330 GHz leads without exception to a larger standard deviation compared to 220 GHz. This result is not surprising as the wavelength reduces with increasing frequency, resulting in a larger phase deviation given a fixed radial error. Secondly, the aluminum extension hook outperforms its polycarbonate counterpart in terms of phase stability, due to its increased mechanical stiffness and the resulting decreased radial error Δr. Finally, larger elevation angles appear to show an increased phase deviation for both materials and frequencies. This can be explained by considering that the bearing of the elevation axis is located at $\theta = 0°$, which means larger elevation angles increase the distance between bearing and receiver, resulting in an increased effect of backlash. If one wanted to counteract this deviation from the bearing tolerances, the extension of the elevation measurement (cf. Fig. 4) could be utilized.

Compared to the findings for the phase above, Fig. 8 (b), shows no dependency of frequency, angle, or chosen material. As explained above, the amplitude fading due to mechanical deviations in the radial direction and cable bends is negligible, as shown by the standard deviation of the amplitude.

Since the phase measurement is in general possible, a more comprehensive investigation of the phase information is necessary. If the open-ended waveguide is approximated as an aperture which features the TE_{10}-mode within an infinite ground-plane, the far-field can be calculated analytically by the Fourier-transform method [31]. Given the width of the waveguide a and its height b as well as the wavenumber $k_0 = 2\pi/\lambda_0$ in free space, one obtains for large distances

$$\frac{\boldsymbol{E}(r,\theta,\varphi=0)}{\mathrm{j}k_0 ab\,E_0} = -\frac{\mathrm{e}^{-\mathrm{j}k_0 r}}{\pi^2 r}\,\mathrm{sinc}\left(\frac{k_0 b\sin\theta}{2}\right)\hat{\boldsymbol{\theta}}, \quad (2)$$

$$\frac{\boldsymbol{E}\left(r,\theta,\varphi=\frac{\pi}{2}\right)}{\mathrm{j}k_0 ab\,E_0} = \frac{\mathrm{e}^{-\mathrm{j}k_0 r}}{r}\,\frac{\cos\left(\frac{k_0 a\sin\theta}{2}\right)\cos\theta}{\pi^2-(k_0 a\sin\theta)^2}\hat{\boldsymbol{\varphi}}, \quad (3)$$

where the phase of each component does exclusively depend on the radius r, but neither on the azimuth angle φ nor on the elevation angle θ. Here, the $\mathrm{sinc}(x)$-function refers to $\sin(x)/x$. Although this approximation does neglect the effects of the obviously finite waveguide flange with its holes, one would expect that the phase over the main lobe of the radiated beam from the open-ended waveguide is relatively constant. Fig. 9 (a) shows an overlay of the phases of all 70

TABLE 3. Calculated distance between origin and phase-center.

Frequency f	Distance in x Δx	Distance in y Δy	Distance in z Δz
220 GHz	$-101.1\,\mu$m	$-307.7\,\mu$m	$-420.3\,\mu$m
250 GHz	$-110.3\,\mu$m	$-302.7\,\mu$m	$-126.2\,\mu$m
330 GHz	$-105.9\,\mu$m	$-306.8\,\mu$m	$-144.7\,\mu$m

TABLE 4. Parameter settings of the VNA for radiation pattern measurements.

Start Freq. f_{Start}	Stop Freq. f_{End}	Freq. Step (2D/3D) Δf_{2D}	Δf_{3D}	Meas. Bandwidth f_{BW}
220 GHz	330 GHz	0.5 GHz	5 GHz	10 Hz

measurements for the upper and lower frequency band. Apart from the small deviations between the repetitively carried out measurements, one can recognize a tendency of decreasing phase angle with increasing elevation angle θ. This means that the electrical path length between transmitting antenna and receiver is shorter for $\theta = 0°$ compared to e.g. $\theta = 50°$, which would imply an undesired shift between waveguide-center and origin. To evaluate this shift, a method to obtain the phase pattern of an antenna where the origin is virtually shifted to another position is presented in [32]. These phase patterns are referred to as the corrected phase pattern, where the correction is carried out for different origin positions. In a 3D global search, the corrected phase pattern of different origin-positions can be evaluated weighting the occurring path differences with the wavenumber [33]. The position with the smoothest, i.e. most constant antenna pattern will be considered the phase center of the antenna. To evaluate the different phase patterns, the relative phase deviation from the average phase is weighted with the power given by the amplitude pattern. By doing so, weak parts of the radiation pattern or even nulls will not disturb the calculation of the phase center.

This method has been applied to the 3D radiation pattern, which will be presented in Section VI. Precisely speaking, a domain of $0° \leq \varphi \leq 360°$ and $0° \leq \theta \leq 50°$ in steps of 5° and 2° for φ and θ, respectively, was measured for both components E_φ and E_θ. The method was applied to the E_x component calculated from the above mentioned measured components, as this component is assumed to be the dominant one within the main lobe of the radiation pattern given the x-polarization of the rectangular waveguide. As a result, the distances between phase-center and origin was calculated and is given in Table 3, and the distance calculated for 250 GHz has been applied to the measured phases from Fig. 9 (a), resulting in the phase-center corrected phases depicted in Fig. 9 (b). Compared to the originally measured phases, the trend of the corrected phases behaves admirably constant. The calculated distance is practically constant for the x and y direction, representing the distance between the manually adjusted center of the waveguide and the origin of the spherical measurement system. Fluctuations of the phase center offset in z-direction have been calculated before for horn antennas [34] and are thus assumed to be linked to the transition between guided and radiated wave, which has been assumed in a strongly simplified manner by the aperture approach yielding the result in (2) and (3). Compared to the positioning of the antenna utilizing the laser pointer (cf. Fig. 1) and the method of comparing the time-domain pulse width of the black arc (cf. Fig. 6), this method is considered the most precise for the determination of the origin of the system. At first, the laser pointer was adjusted manually, however it indicates the approximate origin directly, without further measurements involved. Furthermore, the comparison of the time-domain pulse widths relies on large bandwidth, to obtain a high temporal resolution, which results in relatively long sweep times. However, both methods mentioned above can be utilized during or prior to the measurement. The phase-center calculation relies on much more samples, as it operates on all samples of the radiation pattern, and can be carried out only post-measurement for each frequency independently. Since there has been no calibration and no reference-plane measurement carried out, the absolute offsets of the phases cannot be interpreted. These depend, apart from the distance between transmitter and receiver, also on the utilized cable lengths and the internal structure of the frequency converters. In total, this section has shown that the spherical positioning system presented is capable of achieving measurement data with high repeatability, and providing additional to the often used amplitude information the very sensitive phase information.

VI. OPEN-ENDED WAVEGUIDE MEASUREMENT

To prove the suitability of the measurement system, this section presents the measured radiation pattern of an open-ended rectangular waveguide linking the measurement process to an interpretable outcome and compares it to a full-wave FDTD simulation result of the waveguide calculated by EMPIRE XPU.

With the open-ended waveguide remaining in the origin as the antenna under test, three measurements, namely a gain over frequency measurement at broadside, 2D cut planes, and a full 3D radiation pattern measurement have been carried out. In order to allow for fast measurements and reduce the amount of data, the frequency step size was increased slightly for the 2D measurements and further for the 3D measurements according to Table 4. However, the measurement bandwidth was decreased to allow for more averaging in the time-domain.

At first, the realized gain in broadside direction ($\theta = 0°$) has been measured with the VNA parameters utilized for the 2D measurements. The gain resulting from evaluating (1) is depicted in Fig. 10 in comparison with the solution from the FDTD full-wave simulation of EMPIRE XPU. One can clearly see that the general behavior, as well as the absolute gain of the open-ended waveguide, have been determined in good agreement throughout the whole frequency band. The deviations between both plots are assumed

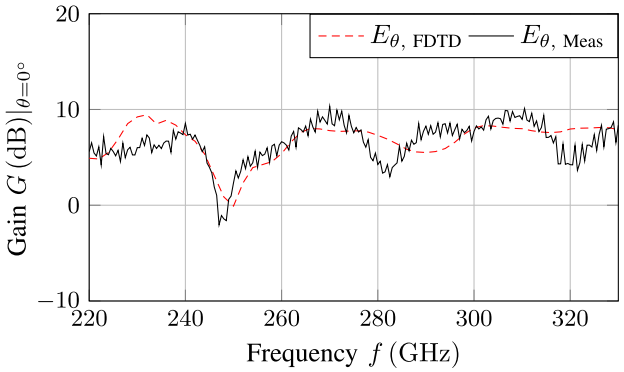

FIGURE 10. Realized gain of the open-ended waveguide over the whole waveguide band in the broadside direction. The result from the FDTD simulation from EMPIRE XPU is given as well.

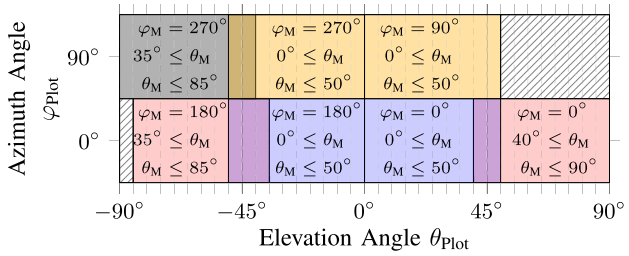

FIGURE 11. Lookup diagram linking the measured azimuth and elevation domains specified by $\varphi_{\mathbf{M}}$ and $\theta_{\mathbf{M}}$ with the domain utilized in 2D polar radiation pattern $\varphi_{\mathbf{Plot}}$, $\theta_{\mathbf{Plot}}$. The ranges of the initial measurement are drawn in blue and orange, the ones from the extended receiver position in red and gray, and the regions which cannot be measured due to collisions are hatched.

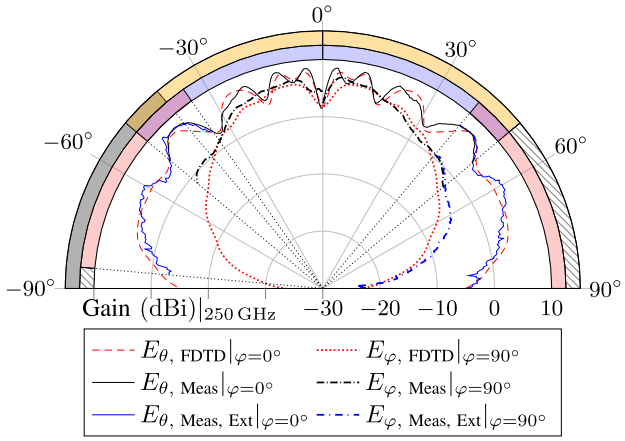

FIGURE 12. Polar radiation pattern of the co-polarization for E- and H-plane comparing the measured results with an FDTD simulation calculated with EMPIRE XPU. The shaded region at the outermost arch corresponds to the measurable regions highlighted in Fig. 11.

TABLE 5. Measured 3D azimuth and elevation domain.

Meas. Type	Elevation Start	Elevation Step	Elevation Stop	Azimuth Start	Azimuth Step	Azimuth Stop
	θ_{Start}	$\Delta\theta$	θ_{Stop}	φ_{Start}	$\Delta\varphi$	φ_{Stop}
Initial	0°	2°	50°	0°	5°	355°
Extended	35°	5°	85°	185°	5°	360°

to be mainly caused by the modeling of the open-ended waveguide within the FDTD simulation. It is presumed that the holes, threads, the chamfered edges at the flange, and the shape of waveguide borders need to be modeled for the present waveguide flange, and not solely based on the available technical drawings for the UG387 waveguide flange.

To enable the comparison of the radiation pattern, the 2D measurement was carried out utilizing 4 elevation cut planes, allowing to display both the $\boldsymbol{E}$-plane (x-z-plane, here referred to $\varphi = 0°$) and the $\boldsymbol{H}$-plane (y-z-plane, here referred to $\varphi = 90°$). The different ranges measured are shown in Fig. 11 sorted to their corresponding plot ranges. To obtain one combined plot of two cut planes comprising all measurements carried out, the different measurement results are stitched together partly overlapping. The hatched regions cannot be measured without further modification of the measurement setup, as a measurement in these regions would result in collisions of the far-field receiver with either the large area manipulator of the left hand side frequency converter (cf. Fig. 4 (a) - $\varphi = 0°$ and $\theta < -85°$) or with the microscope ($\varphi = 90°$ and $\theta > 50°$). The resulting 2D far-field-pattern for 250 GHz is shown in Fig. 12, comparing the co-polarization for the measured and $\boldsymbol{E}$- and $\boldsymbol{H}$-plane measurements with the FDTD solution simulated by EMPIRE XPU. To visualize the overlapping regions, the measurements utilizing the extended theta range are labeled explicitly. Furthermore, the different achievable measurement ranges are visualized as outermost arches utilizing the color key of Fig. 11 to emphasize the link between both plots. The measurement results are in very good agreement with the outcome of the FDTD simulation throughout the overall covered elevation range. Additionally, the overlapping regions of the different measurements are in nearly perfect agreement, which made it necessary to use different colored plotlines to distinguish them.

Finally, a full 3D measurement has been carried out. The measured ranges in elevation and azimuth direction need to be covered twice with different orientations of the receiver, resulting in data of both the E_φ and E_θ-component. A pointwise superposition of the resulting E_φ and E_θ-components can be performed after the measurement in order to achieve a complex vector field representing the measurement. Additionally, this vector field can be projected on any cartesian (or arbitrarily defined) direction. In such a way, not only the norm $||\boldsymbol{E}||$, but also single components as E_x could be extracted, and for example, used to perform a phase center calculation. In order to perceive a measurement result that visually represents the upper hemisphere, two measurement ranges, one initial measurement representing the dome of the radiation pattern and one extended measurement representing the margin, are combined in a similar manner as in the 2D case. The measurement points with respect to the spherical coordinate system are given in Table 5. It should be pointed out that the extended measurement only covers points within

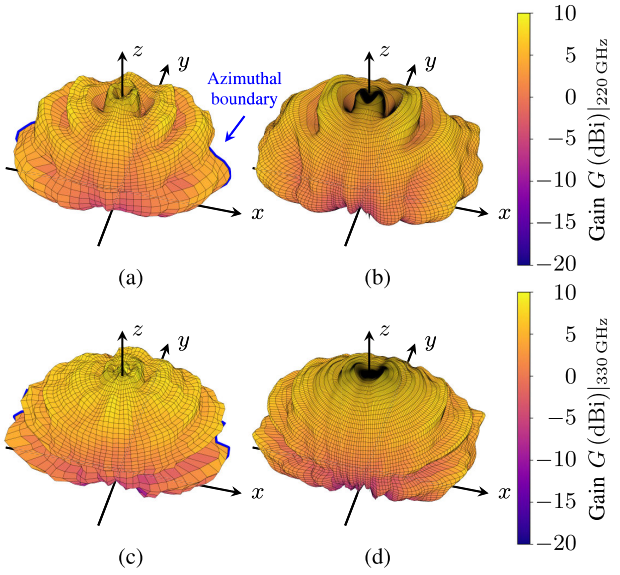

FIGURE 13. 3D radiation pattern for 220 GHz (a, b) and 330 GHz (c, d). The radiation pattern on the left hand side (a, c) were measured with the presented measurement system, the results from a full-wave FDTD simulation calculated with EMPIRE XPU are shown on the right hand side (b, d). The measured results were obtained within the domain given in Table 5, the azimuthal boundaries of the extended domain are highlighted by the blue corners.

$185° \leq \varphi \leq 360°$ to prevent collisions with the microscope, as explained above. The duration of the initial measurement is roughly 5 h per polarization, the extended measurement is faster due to the reduced resolution in elevation direction and the reduced number of points in azimuth, resulting in a total measurement time of roughly 14 h. Whereas the 2D radiation pattern presented above depicted a frequency of 250 GHz centered within the WR3.4 band, the 3D radiation pattern shown in Fig. 13 represent the lower and upper bound of the band, namely 220 GHz and 330 GHz. Again, both the absolute gain and the general shape of the radiation pattern are in very good agreement when comparing simulation and measurement. The reduced elevation resolution chosen for the extended range can be clearly recognized by the coarser pattern. Additionally, the missing azimuthal range $0° < \varphi < 180°$ for the extended measurement is highlighted by the blue line and labeled as azimuthal boundary, emphasizing the limitation of the carried out measurement. If the microscope was demounted, which is in general possible due to a quick-change adaptor, an even wider elevation range could be measured for $0° < \varphi < 180°$.

Recapitulating this section, the presented measurement results show an excellent agreement of gain over frequency, 2D-, and 3D radiation pattern with full-wave simulation results and therefore confirm the usability and reliability of the presented mm-wave antenna measurement system.

VII. CONCLUSION

An on-wafer mm-wave antenna measurement system providing amplitude and phase information has been designed, set up and characterized. Its inherent positioning in spherical coordinates allows for direct far-field measurements of the upper hemisphere, and although it is limited in the elevation range, this limitation can be conquered by mechanical extension as well as stitching of measurement results, as shown successfully in this paper. It utilizes mostly plastics within the upper hemisphere to reduce reflections, whereas a self-characterization has been carried out by the system in terms of a SAR-based reflection analysis. The system itself allows for the characterization of waveguide- or probe-fed antennas and partially integrated systems. In general, by applying corresponding frequency converters, the system allows for other commonly used waveguide bands increasing the possible frequency range, where especially the self-characterizations presented here can be performed in the same manner. Again, the strictly reduced use of metal parts in the upper hemisphere reduces the dependency on available absorbers.

In future work, both the characterization of on-chip antennas as well as increased frequency measurements will be carried out. The limitations and challenges of on-wafer measurements need to be evaluated separately after this work has shown the general capabilities of the system. Considerable attention needs to be paid on correct contacting the on-wafer pads, the near-and far-field influence of the wafer probe as well as the long-term stability of the measurement system for long-lasting measurements. The modularity of the system combined with the optical table allows for both fast and reliable substitution of measurement devices. Finally, the characterization at multiple frequency bands to measure sub-harmonic or harmonic signal leakage, for example, is conceivably possible.

ACKNOWLEDGMENT

The authors are grateful for the collaborative design process of the spherical positioning system provided by Demcon Systec Industrial Systems.

REFERENCES

[1] R. Pilard, S. Montusclat, D. Gloria, F. Le Pennec, and C. Person, "Dedicated measurement setup for millimetre-wave silicon integrated antennas: BiCMOS and CMOS high resistivity SOI process characterization," in *Proc. 3rd Eur. Conf. Antennas Propag.*, Berlin, Germany, Mar. 2009, pp. 2447–2451.

[2] S. Ranvier, M. Kyrö, C. Icheln, C. Luxey, R. Staraj, and P. Vainikainen, "Compact 3-D on-wafer radiation pattern measurement system for 60 GHz antennas," *Microw. Opt. Technol. Lett.*, vol. 51, no. 2, pp. 319–324, 2009.

[3] X. Qing and Z. N. Chen, "Measurement setups for millimeter-wave antennas at 60/140/270 GHz bands," in *Proc. Int. Workshop Antenna Technol., Small Antennas, Novel EM Struct. Mater., Appl. (iWAT)*, Sydney, NSW, Australia, Mar. 2014, pp. 281–284.

[4] M. Neshat, D. M. Hailu, M.-R. Nezhad-Ahmadi, G. Z. Rafi, and S. Safavi-Naeini, "Gain measurement of embedded on-chip antennas in mmW/THz range," *IEEE Trans. Antennas Propag.*, vol. 60, no. 5, pp. 2544–2549, May 2012.

[5] D. Titz, F. Ferrero, C. Luxey, and G. Jacquemod, "A novel fully-automatic 3D radiation pattern measurement setup for 60 GHz probe-fed antennas," in *Proc. IEEE Int. Symp. Antennas Propag. (APSURSI)*, Spokane, WA, USA, Jul. 2011, pp. 3121–3124.

[6] A. Bisognin, D. Titz, F. Ferrero, G. Jacquemod, R. Pilard, F. Gianesello, D. Gloria, C. Laporte, H. Ezzeddine, D. Lugara, and C. Luxey, "Probe-fed measurement system for F-band antennas," in *Proc. 8th Eur. Conf. Antennas Propag. (EuCAP)*, The Hague, The Netherlands, Apr. 2014, pp. 722–726.
[7] S. Beer and T. Zwick, "Probe based radiation pattern measurements for highly integrated millimeter-wave antennas," in *Proc. 4th Eur. Conf. Antennas Propag.*, Barcelona, Spain, Apr. 2010, pp. 1–5.
[8] H. Gulan, S. Beer, S. Diebold, C. Rusch, A. Leuther, I. Kallfass, and T. Zwick, "Probe based antenna measurements up to 325 GHz for upcoming millimeter-wave applications," in *Proc. Int. Workshop Antenna Technol. (iWAT)*, Karlsruhe, Germany, Mar. 2013, pp. 228–231.
[9] L. Boehm, S. Pledl, F. Boegelsack, M. Hitzler, and C. Waldschmidt, "Robotically controlled directivity and gain measurements of integrated antennas at 280 GHz," in *Proc. Eur. Microw. Conf. (EuMC)*, Paris, France, Sep. 2015, pp. 315–318.
[10] T. Zwick, C. Baks, U. R. Pfeiffer, D. Liu, and B. P. Gaucher, "Probe based MMW antenna measurement setup," in *Proc. IEEE Antennas Propag. Soc. Symp.*, Jun. 2004, pp. 747–750.
[11] T. Ito, Y. Tsutsumi, S. Obayashi, H. Shoki, and T. Morooka, "Radiation pattern measurement system for millimeter-wave antenna fed by contact probe," in *Proc. Eur. Microw. Conf. (EuMC)*, Rome, Italy, Sep./Oct. 2009, pp. 1543–1546.
[12] D. Novotny, M. Francis, R. Wittmann, J. Gordon, J. Guerrieri, and A. Curtin, "Multi-purpose configurable range for antenna testing up to 220 GHz," in *Proc. 10th Eur. Conf. Antennas Propag. (EuCAP)*, Davos, Switzerland, Apr. 2016, pp. 1–3.
[13] A. Arboleya, Y. Alvarez, and F. Las-Heras, "Millimeter and submillimeter planar measurement setup," in *Proc. IEEE Antennas Propag. Soc. Int. Symp. (APSURSI)*, Lake Buena Vista, FL, USA, Jul. 2013, pp. 1–2.
[14] H. Gulan, C. Luxey, and D. Titz, "nmm-wave sub-mm-wave antenna measurement," in *Handbook Antenna Technologies*, Z. N. Chen, Ed. Singapore: Springer, 2014, pp. 1–40.
[15] R. Simons, "Novel on-wafer radiation pattern measurement technique for MEMS actuator based reconfigurable patch antennas," NASA, Washington, DC, USA, Tech. Rep. TM-2002-211816, Oct. 2002.
[16] D. J. van Rensburg and S. F. Gregson, "Parametric study of probe positioning errors in articulated spherical near-field test systems for mm-wave applications," in *Proc. IEEE Conf. Antenna Meas. Appl. (CAMA)*, Nov. 2014, pp. 1–4.
[17] M. Fakharzadeh, "Antenna measurement in probe station," in *Proc. IEEE Antennas Propag. Soc. Int. Symp. (APSURSI)*, Jul. 2014, pp. 293–294.
[18] D. Titz, R. Pilard, F. Ferrero, F. Gianesello, D. Gloria, G. Jacquemod, and C. Luxey, "Improved measurement accuracy of probe-Fed mm-wave antennas using the three Γ method," *IEEE Antennas Wireless Propag. Lett.*, vol. 13, pp. 103–105, 2014.
[19] K. Mohammadpour-Aghdam, S. Brebels, A. Enayati, R. Faraji-Dana, G. A. E. Vandenbosch, and W. DeRaedt, "RF probe influence study in millimeter-wave antenna pattern measurements," *Int. J. RF Microw. Comput.-Aided Eng.*, vol. 21, no. 4, pp. 413–420, 2011.
[20] L. Boehm, M. Hitzler, F. Roos, and C. Waldschmidt, "Probe influence on integrated antenna measurements at frequencies above 100 GHz," in *Proc. 46th Eur. Microw. Conf. (EuMC)*, London, U.K., Oct. 2016, pp. 552–555.
[21] Y. Fu, T. P. Vuong, L. Dussopt, and F. Ndagijimana, "Characterization of integrated antennas at millimeter-wave frequencies," in *Proc. 5th Eur. Conf. Antennas Propag.*, Rome, Italy, Apr. 2011, pp. 160–163.
[22] Z.-M. Tsai, Y.-C. Wu, S.-Y. Chen, T. Lee, and H. Wang, "A V-Band on-wafer near-field antenna measurement system using an IC probe station," *IEEE Trans. Antennas Propag.*, vol. 61, no. 4, pp. 2058–2067, Apr. 2013.
[23] J. Murdock, E. Ben-Dor, F. Gutierrez, and T. S. Rappaport, "Challenges and approaches to on-chip millimeter wave antenna pattern measurements," in *IEEE MTT-S Int. Microw. Symp. Dig.*, Baltimore, MD, USA, Jun. 2011, pp. 1–4.
[24] D. Titz, F. Ferrero, P. Brachat, G. Jacquemod, and C. Luxey, "Efficiency measurement of probe-fed antennas operating at millimeter-wave frequencies," *IEEE Antennas Wireless Propag. Lett.*, vol. 11, pp. 1194–1197, 2012.
[25] M. Hitzler, S. Bader, and C. Waldschmidt, "Key aspects of robot based antenna measurements at millimeter wave frequencies," in *Proc. 8th Eur. Conf. Antennas Propag. (EuCAP)*, Apr. 2014, pp. 392–396.
[26] J. Akkermans, R. van Dijk, and M. Herben, "Millimeter-wave antenna measurement," in *Proc. Eur. Microw. Conf.*, Munich, Germany, Oct. 2007, pp. 83–86.
[27] A. F. Yegulalp, "Fast backprojection algorithm for synthetic aperture radar," in *Proc. IEEE Radar Conf. Radar Next Millennium*, Waltham, MA, USA, Apr. 1999, pp. 60–65.
[28] L. Boehm, F. Boegelsack, M. Hitzler, S. Wiehler, and C. Waldschmidt, "Accuracy evaluation for antenna measurements at mm-wave frequencies," in *Proc. 10th Eur. Conf. Antennas Propag. (EuCAP)*, Apr. 2016, pp. 1–5.
[29] D. J. van Rensburg and G. Hindman, "An overview of near-field sub-millimeter wave antenna test applications," in *Proc. 14th Conf. Microw. Techn.*, Apr. 2008, pp. 1–4.
[30] J. Vancl, P. Cerny, Z. Skvor, and M. Mazanek, "Evaluation and correction of cable phase stability in high frequency near-field measurement," in *Proc. 14th Conf. Microw. Techn.*, Apr. 2008, pp. 1–4.
[31] R. E. Collin, "Aperture-type antennas," in *Antennas and Radiowave Propagation*. New York, NY, USA: McGraw-Hill, 1985.
[32] N. Basta, A. Konovaltsev, and L. Greda, "Phase centre determination on the basis of far-field measurements," *Coordinates*, vol. 6, no. 8, pp. 7–10, Aug. 2010.
[33] Y. Chen and R. G. Vaughan, "Determining the three-dimensional phase center of an antenna," in *Proc. XXXIth URSI Gen. Assem. Sci. Symp. (URSI GASS)*, Aug. 2014, pp. 1–4.
[34] Y. G. Wang, J. Wang, Z. Q. Zhao, and J. Y. Yang, "A novel method to calculate the phase center of antennas," *J. Electromagn. Waves Appl.*, vol. 22, nos. 2–3, pp. 239–250, Jan. 2008.

BENEDIKT SIEVERT (Member, IEEE) was born in Krefeld, Germany. He received the B.Sc. and M.Sc. degrees in electrical engineering/high-frequency systems from the University of Duisburg-Essen, in 2017 and 2019, respectively.

Since 2017, he has been a member of the Laboratory of General and Theoretical Electrical Engineering, University of Duisburg-Essen. His research interests include mm-wave on-chip antennas, electromagnetic metamaterials, theoretical, and computational electromagnetics.

JAN TARO SVEJDA (Member, IEEE) received the B.Sc. degree in electrical engineering from the University of Applied Science, Düsseldorf, Germany, in 2008, and the M.Sc. and Dr.-Ing. degrees in electrical engineering and information technology from the University of Duisburg-Essen, Duisburg, Germany, in 2013 and 2019, respectively. His research work is in the field of X-nuclei-based magnetic resonance imaging. He is currently a Research Assistant with the Department of General and Theoretical Electrical Engineering, University of Duisburg-Essen, where he is involved in teaching several lectures and courses mainly in the field of electrical engineering. His general research interests include all aspects of theoretical and applied electromagnetics, currently focusing on medical applications, electromagnetic metamaterials, and scientific computing methods.

DANIEL ERNI (Member, IEEE) received the Diploma degree in electrical engineering from the University of Applied Sciences in Rapperswil (HSR), in 1986, the Diploma degree in electrical engineering from ETH Zürich, in 1990, and the Ph.D. degree in laser physics from ETH Zürich, in 1996. Since 1990, he has been with the Laboratory for Electromagnetic Fields and Microwave Electronics, ETH Zürich. From 1995 to 2006, he was the Founder and the Head of the Communication Photonics Group, ETH Zürich. Since October 2006, he has been a Full Professor of general and theoretical electrical engineering with the University of Duisburg-Essen, Germany. His current research interests include optical interconnects, nanophotonics, plasmonics, advanced solar cell concepts, optical and electromagnetic metamaterials, RF, mm-wave and THz engineering, biomedical engineering, bioelectromagnetics, marine electromagnetics, computational electromagnetics, multiscale and multiphysics modeling, numerical structural optimization, and science and technology studies (STS). He is a Co-Founder of the spin-off company airCode on flexible printed RFID technology. He is a Fellow of the Electromagnetics Academy, a member of the Center for Nanointegration Duisburg-Essen (CeNIDE), and a member of the Swiss Physical Society (SPS), of the German Physical Society (DPG), and of the Optical Society of America (OSA).

ANDREAS RENNINGS (Member, IEEE) received the degree in electrical engineering from the University of Duisburg-Essen, Germany, the Diploma degree from the University of California at Los Angeles, and the Dipl.-Ing. and Dr.-Ing. degrees from the University of Duisburg-Essen, in 2000 and 2008, respectively. From 2006 to 2008, he was with IMST GmbH, Kamp-Lintfort, Germany, where he was an RF Engineer. Since 2008, he has been a Senior Scientist and a Principal Investigator with the Laboratory for General and Theoretical Electrical Engineering, University of Duisburg-Essen. His general research interests include all aspects of theoretical and applied electromagnetics, currently with a focus on medical applications and on-chip millimeter-wave/THz antennas. He received several awards, including a Student Paper Price at the 2005 IEEE Antennas and Propagation Society International Symposium and the VDE-Promotionspreis 2009 for the dissertation.